Research Article

Modified P&O MPPT algorithm for optimal power extraction of five-phase PMSG based wind generation system

Hossam H. H. Mousa[1] · Abdel-Raheem Youssef[1] · Essam E. M. Mohamed[1]

Abstract
In this study, the maximum power point tracking (MPPT) performance is investigated based on variable-speed wind energy conversion system below the rated wind speed. The proposed modified perturb and observe (MPO) MPPT enhances the initial speed-tracking accuracy and eliminates the oscillations level. The MPO employs four sectors operation using a variable-speed step sizes by comparing the new suggesting curve with the P–ω curve. The system is described as a large-scale five-phase permanent magnet synchronous generator (PMSG) which is grid connected through a back-to-back converter (BTBC) and Dc-link capacitor. The field-oriented control (FOC) is applied in the machine-side converter (MSC) to extract the optimal generated power using the proposed MPPT algorithm. Moreover, the voltage-oriented control (VOC) is applied in the grid-side converter (GSC) to regulate the Dc-link voltage and inject active power with unity power factor. The simulation results depict the superior performance of the MPO over the conventional P&O. The performance of the proposed control scheme is validated using MATLAB/SIMULINK program.

Keywords Modified P&O · WECS · MPPT · Five-phase PMSG · PI controller

List of symbols

T_e	Electromagnetic torque
T_m	Mechanical torque
p	Number of pair poles
ψ	Flux linkage
f	Viscous damping coefficient
J	Moment of inertia
ω_m	Turbine rotor angular speed
ω_{ref}	Reference rotor speed
ω_e	Electric angular rotor speed
C_p	Power coefficient
β	Pitch angle
λ	Tip speed ratio
ρ	Air density (Kg/m^3)
R	Turbine radius (m)
V_{wind}	Wind speed (m/s)
$A \approx \pi R^2$	Turbine blades swept area (m^2)
$V_{d1,q1,d3,q3}$	d–q stator voltage components
$i_{d1,q1,d3,q3}$	d–q stator current components
$\psi_{d1,q1,d3,q3}$	d–q flux linkage components
$L_{d1,q1,d3,q3}$	d–q stator inductance components
PF	Power factor
V_{ia}, V_{ib}, V_{ic}	GSC inverter voltages
i_{ia}, i_{ib}, i_{ic}	Currents through filters
V_{ga}, V_{gb}, V_{gc}	GSC voltages
V_{gd}, V_{gq}	d–q axis grid components
I_c	Dc-link capacitor current
P_e	Output MSC power
P_g	Delivering grid power
Q_g	Reactive grid power

List of abbreviations

PLL	Phase-locked loop
WECS	Wind energy conversion system
PMSG	Permanent magnet synchronous generators
MSC	Machine-side converter
GSC	Grid-side converter
BTBC	Back-to-back converters

✉ Hossam H. H. Mousa, H.Herzallah@eng.svu.edu.eg; Abdel-Raheem Youssef, A.yousaf@eng.svu.edu.eg; Essam E. M. Mohamed, Essam.mohamed@eng.svu.edu.eg | [1]Department of Electrical Engineering, South Valley University, Qena, Egypt.

SN Applied Sciences (2019) 1:838 | https://doi.org/10.1007/s42452-019-0878-5

Received: 6 April 2019 / Accepted: 2 July 2019 / Published online: 8 July 2019

FSWT	Fixed-speed wind turbine
VSWT	Variable-speed wind turbine
SCIG	Squirrel-cage induction generator
DFIG	Doubly fed induction generator
FTC	Fault-tolerant capability
LVRT	Low-voltage ride through
FOC	Field-oriented control
VOC	Voltage-oriented control
MPPT	Maximum power point tracking
SVPWM	Space vector pulse width modulation
TSR	Tip speed ratio
IPC	Indirect power controller
DPC	Direct power controller
PSF	Power signal feedback
OT	Optimal torque
HCS	Hill climbing search
P&O	Perturb and observe
INC	Incremental conductance
ORB	Optimum relation based
CPO	Conventional P&O
MPO	Modified P&O

1 Introduction

Increasing global demand of electrical energy and the need for the fossil fuels substitution, which causes greenhouse effect, carbon emission and environmental pollution problems are the main stimuli for clean energy growth [1]. Renewable energy sources (RESs), such as wind, solar, hydropower and geothermal, are the accessible way to eliminate these drawbacks [2]. Among them, wind energy is considered one of the most important RESs that will supply, as expected, 20% of the global energy by 2030 [3].

To cope with the increasing development of the wind energy conversion system (WECS) and meet the energy requirements, two main categories of wind turbines have been equipped in the WECS [3, 4]. The WECS consists of the fixed-speed wind turbine (FSWT), which is simple and less costly but also needs multistage gearboxes. The variable-speed wind turbine (VSWT) has the ability to operate at maximum power at various wind speeds [5]. Many generator types have been applied in the WECS through the global marketing such as the squirrel-cage induction generators (SCIGs), the doubly fed induction generators (DFIGs) and the permanent magnet synchronous generators (PMSGs) [6, 7]. Although DFIGs, among various generators types, have strong commercial solutions in the WECS [5]; researchers, recently, turned to implement the PMSG in the WECS according to its features such as good performance with high efficiency, high power density and high accuracy [4]. Furthermore, the wide-ranging controllability of extreme power extracting at different wind speeds as well as the absence of gearboxes and the DC exciting system increase the WECS efficiency by 10% [8]. At a recent time, many researchers study the applications of multi-phase machines to minimize the switching current for each phase and torque pulsation, and fault-tolerant capability (FTC) enhancement [9, 10]. Several topologies are utilized in the WECS such as the dual three-phase machines [11, 12] and the six-phase machines [13, 14]; however, they suffer from many drawbacks such as the control systems complexity and using costly converters. Now, the five-phase PMSG expands to several trends such as marine turbines [15], small-scale WECS [16] and large-scale WECS [17].

To attain all available wind power, the optimal rotor speed is compared to the actual rotor speed in the speed closed control loop, according to the wind speed variations. At different wind speeds, the rotational speed of the generator must be regulated to obtain the maximum generated power at the VSWT using the maximum power point tracking (MPPT) algorithms. In order to increase the attainable power from the VSWT, MPPT techniques are, generally, assorted into indirect power controller (IPC) and direct power controller (DPC) [5, 18]. The IPC depends on the pre-calculated power from wind speed curves that increases the mechanical power (P_{wind}), whereas the DPC examines directly the output electrical power (P_{ele}) to operate at the MPP. The relationship of P_{wind} and P_{ele} is illustrated in Eq. (1) where η_g and η_c are the efficiencies of the generator and the converter, respectively, according to rotor speed variation [18, 19]. The IPC control has applied three several types of MPPT algorithm such as the tip speed ratio (TSR) [20], the power signal feedback (PSF) and the optimal torque (OT). The TSR algorithm is simple and efficient to regulate the rotor speed. Although, it has a quick response, it is inexact due to the wind turbine (WT) blades turbulence. The PSF and OT need specific parameters of the WT although they do not require an anemometer [19, 21].

The DPC is extensively used to detect the MPP through the wind speed variations by evaluating any power change; also, it provides the simplicity and the flexibility for the WECS [18, 19]. Therefore, DPC algorithms are assorted into the hill climbing search (HCS) or the perturb and observe (P&O), incremental conductance (INC) and optimum relation-based (ORB) MPPT algorithms [5, 9, 22]. The conventional or modified INC algorithms are efficient optimal power extraction techniques as regards the power efficiency [23, 24]. However, the ORB is fast and accurate method, it needs lookup table, which is obtained from optimum relationships information under several system parameters [25, 26]. Among these, the P&O is simple method at any below-rated wind speed which it adjusts the step magnitude relative to the rotor speed variation

through the direction perturb. Additionally, it needs no specific parameters of the WT. The P&O algorithm depends upon varying the rotor speed in steps, observing and analysing the harvest power magnitude and searching the MPP that makes the power-speed curve slope equals zero. The step size in P&O is classified into fixed step and variable step. The conventional P&O (CPO) method is applied the fixed step size, otherwise using the variable step size that lessens the CPO algorithm drawbacks. In the CPO, choosing the step size is earnest problem that affects the WT performance. Therefore, if the small step is selected, the controller response is very slow that causes power losing in transient period. Furthermore, high output power oscillations and reducing system efficiency are the main drawbacks of implementing the large step [5, 18, 19]. Those problems' solutions are represented by using adaptive step size [27–29]. However, many assumptions and implementation arrangements are still required. Moreover, they require calculating k_{opt} at each wind speed; hence, they may utilize incorrect MPP. In [30, 31], the mechanical stress and high WT inertia are reduced via an enhanced techniques over the CPO. However, a constant and exact slope ramp signal with the accurate design is required. Moreover, they involve a low-pass filter which requires accurate design. Researchers implement the anemometer in their proposed algorithms to solve the speed-tracking problems. An efficient variable-step P&O technique is proposed using two stages to obtain the accurate MPP [32]. However, the prior knowledge requirement of WT parameters is the main drawback. On the other hand, the loss-tracking problem in the CPO is solved using an adaptive P&O algorithm that depends upon the optimal power curve in [28, 33, 34].The modified P&O algorithm solves the slow speed-tracking problem by using large step in forward direction and small step in reverse direction [8]. However, this algorithm applies a constant large forward step size which causes steady-state oscillations around the MPP. Another adaptive P&O MPPT algorithm is proposed in [35–37]. An adaptive P&O algorithm is investigated to avoid the drawbacks of other P&O algorithms by using anemometers. The step size is calculated using wind speed data and rate of change in output power. However, the proposed algorithm requires many calculations that increase system complexity [38]. A novel inertial power-based P&O algorithm is proposed for high inertia WT, which a priori knowledge of WT inertia is required [39].

This paper analyse the performance of a proposed modified P&O (MPO) MPPT algorithm that depends upon an adaptive variable step size for grid-tied five-phase PMSG-based WECS. In addition, the FOC is applied in the MSC with adding the MPPT algorithm in order to obtain a maximum available power at any wind speed. On the GSC, the VOC is applied to regulate the voltage of the Dc-link and achieve unity power factor. The main contribution can be summarized as follows:

- This article proposes a modified P&O MPPT algorithm that eradicates limitations of conventional and existing P&O MPPT techniques such as large oscillations and slow tracking speed.
- The strategy depends on the idea of dividing the power-speed curve into four sectors by comparing the power-speed curve and a newly synthesized curve.
- Each sector has a specific step size. For the sectors close to the MPP, small step size is applied. Otherwise, a large step size is applied.
- The proposed MPO algorithm offers high efficiency and fast response at different wind speeds.
- As a result of the proposed MPO algorithm, not only the loss of tracking and wrong directionally problems are evaded, but also the dynamic tracking performance is improved by accurately attainting the MPP with high performance, either in the transient or in the steady-state conditions.
- The proposed MPO algorithm is compared with the conventional P&O MPPT technique to verify the superiority of the proposed technique.
- The proposed MPO algorithm enhances the WECS efficiency by 3.0% over the conventional one.

This paper is arranged as the description of the WECS modelling containing the WT model and the five-phase PMSG in Sect. 2. Section 3 contains the MSC control explanation. In Sect. 4, the CPO and the proposed MPO MPPT are evaluated in detail. In addition, the GSC control and the simulation results with discussion are present in Sects. 5 and 6, respectively. Finally, the conclusion is debated in Sect. 7.

$$P_{ele} = \eta_g \eta_c P_{wind} \quad (1)$$

2 Modelling of wind energy conversion system

The variable-speed WECS configuration based on large-scale five-phase PMSG is illustrated in Fig. 1. It consists of WT directly attached to the prime mover, which is tied to generator rotor shaft. The BTBC ties the five-phase PMSG with the utility grid. The machine-side converter (MSC) is employed to extract the optimal power at wind speed variations. Otherwise, the grid-side converter (GSC) is applied to ensure grid power injection at unit power factor [16, 18, 37].

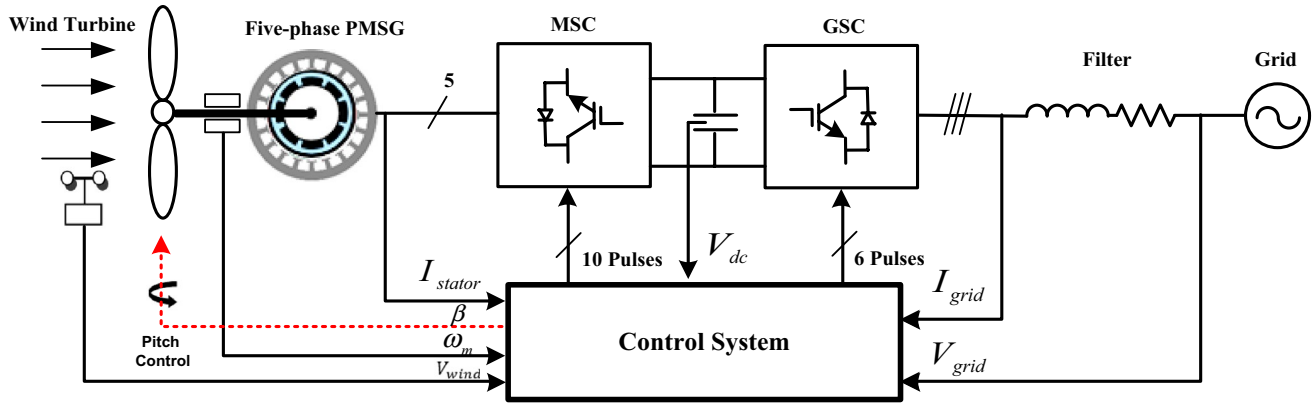

Fig. 1 Grid-connected WECS configuration of PMSG

2.1 Wind turbine model

The different WT characteristics such as mechanical power, tip speed ratio, power coefficient and mechanical torque equations of the VSWT are expressed as surveys in [4, 8, 40]:

$$P_{\mathrm{m}} = C_{\mathrm{p}}(\lambda, \beta)\frac{\rho A}{2}V_{\mathrm{wind}}^{3} \tag{2}$$

where ρ is the air density, β is the pitch angle, A is the swept area of WT blades and V_{wind} is the wind speed.

$$\lambda = \frac{\omega_{\mathrm{m}} R}{V_{\mathrm{wind}}} \tag{3}$$

where ω_{m} is the rotor speed and R is the radius of WT.

$$C_{\mathrm{p}}(\lambda, \beta) = C_1\left(\frac{C_2}{\lambda_i} - C_3\beta - C_4\right)\mathrm{e}^{\frac{-C_5}{\lambda_i}} + C_6\lambda \tag{4}$$

The WT coefficients C_1–C_6 is represented in "Appendix 1"

$$\lambda_i^{-1} = (\lambda + 0.08\beta)^{-1} - 0.035\left(1 + \beta^3\right)^{-1} \tag{5}$$

$$T_{\mathrm{m}} = \frac{P_{\mathrm{m}}}{\omega_{\mathrm{m}}} \tag{6}$$

From previous equations, it is cleared that the TSR depends on the rotor speed and the operating wind speed. In addition, the mechanical power is expressed as a function of the power coefficient and the wind speed at optimum pitch angle. It is also obvious that the optimum value of P_{m} is only acquired when the rate change of $\frac{\mathrm{d}P_{\mathrm{m}}}{\mathrm{d}\omega}$ is zero. To achieve the optimum power, the condition is applied to Eq. (2) as follows:

$$\frac{\mathrm{d}P_{\mathrm{m}}}{\mathrm{d}\omega_{\mathrm{m}}} = 0.5\rho A V_{\mathrm{wind}}^{3}\frac{\mathrm{d}C_{\mathrm{p}}(\lambda, \beta)}{\mathrm{d}\omega_{\mathrm{m}}} \tag{7}$$

when β is optimum (equals zero), then the value of C_{p} is a function of λ only.

The value of $\frac{\mathrm{d}C_{\mathrm{p}}}{\mathrm{d}\omega_{\mathrm{m}}}$ is given as:

$$\frac{\mathrm{d}C_{\mathrm{p}}}{\mathrm{d}\omega_{\mathrm{m}}} = \frac{\mathrm{d}C_{\mathrm{p}}}{\mathrm{d}\lambda_i} * \frac{\mathrm{d}\lambda_i}{\mathrm{d}\omega_{\mathrm{m}}} \tag{8}$$

Then,

$$\frac{\mathrm{d}P_{\mathrm{m}}}{\mathrm{d}\omega_{\mathrm{m}}} = 0.5\rho A V_{\mathrm{wind}}^{3}\left(\frac{1260}{\lambda_i^3} - \frac{114.39}{\lambda_i^2}\right)\mathrm{e}^{\frac{-21}{\lambda_i}} * \frac{V_{\mathrm{wind}} * R}{\left(V_{\mathrm{wind}} - 0.035R\omega_{\mathrm{m}}\right)^2} \tag{9}$$

To obtain the maximum power condition when $(V_{\mathrm{wind}} - 0.035R\omega_{\mathrm{m}}) \neq 0$, λ_{opt} and $C_{\mathrm{p\_opt}}$ values are 8.1 and 0.48, respectively, as shown in Fig. 4.

The captured power from the VSWT is controlled to work within a specific wind speed range limited by $V_{\mathrm{cut\ in}}$ and $V_{\mathrm{cut\ out}}$. Otherwise, the WT must be stop for safety requirements. Figure 2 is illustrated four regions according the rated power and wind speed range. In Region 1 and Region 4, below $V_{\mathrm{cut\ in}}$ and above $V_{\mathrm{cut\ out}}$, respectively, the WT is not

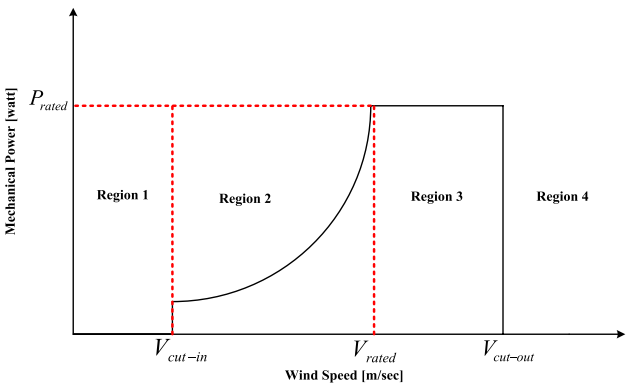

Fig. 2 Turbine operating regions

tied with the utility grid. In Region 2, the MPPT is operating to obtain optimal output power with wind speed range between $V_{\text{cut in}}$ and V_{rated}. The mechanical power is restricted to the rated power in order to keep the WT safe in Region 3 [18, 19].

To harvest maximum captured power from wind, the rotor speed should be regulated at different wind speeds. The efficient WECS control tracks the MPP at any wind velocity change to maximize the output power as shown in Fig. 3. The optimal power condition is attained, while λ, C_p and β are optimal values as shown in Fig. 4 [5, 18].

2.2 Multi-phase PMSG dynamic model

To investigate the dynamic model of the multi-phase PMSG and the d–q components of stator voltages in the synchronous reference frame, the extended Park's transformation are used [36, 41]:

$$\begin{bmatrix} V_{d1} \\ V_{q1} \\ V_{d3} \\ V_{q3} \end{bmatrix} = [R_s] \begin{bmatrix} i_{d1} \\ i_{q1} \\ i_{d3} \\ i_{q3} \end{bmatrix} + \begin{bmatrix} \dot{\lambda}_{d1} - \omega_e \psi_{q1} \\ \dot{\lambda}_{q1} + \omega_e \psi_{d1} \\ \dot{\lambda}_{d3} - 3\omega_e \psi_{q3} \\ \dot{\lambda}_{q3} + 3\omega_e \psi_{d3} \end{bmatrix} \tag{10}$$

where $\dot{\lambda}_{d1} = L_{d1} \frac{di_{d1}}{dt}$, $\dot{\lambda}_{q1} = L_{q1} \frac{di_{q1}}{dt}$, $\dot{\lambda}_{d3} = L_{d3} \frac{di_{d3}}{dt}$ and $\dot{\lambda}_{q3} = L_{q3} \frac{di_{q3}}{dt}$. R_s is the stator resistance matrix, ω_e is the electric angular of rotor speed, i_{d1}, i_{q1}, i_{d3} and i_{q3} are d–q stator current components and L_{d1}, L_{q1}, L_{d3} and L_{q3} are d–q stator inductance components.

The stator flux linkage components can be written as:

$$\psi_{q1} = L_{q1} i_{q1} \tag{11}$$

$$\psi_{d1} = L_{d1} i_{d1} + \psi_1 \tag{12}$$

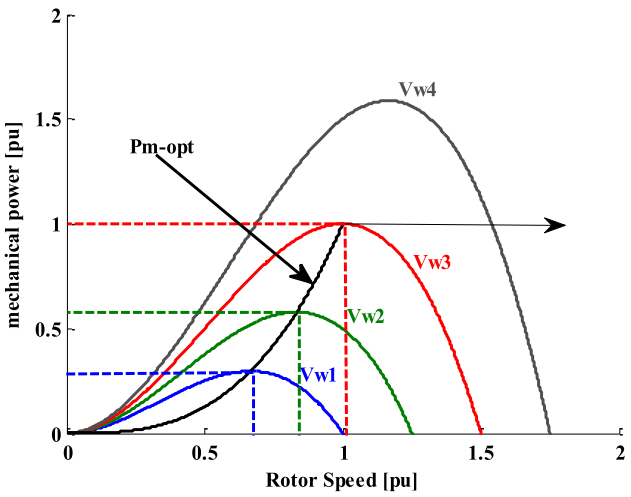

Fig. 3 Turbine power characteristics

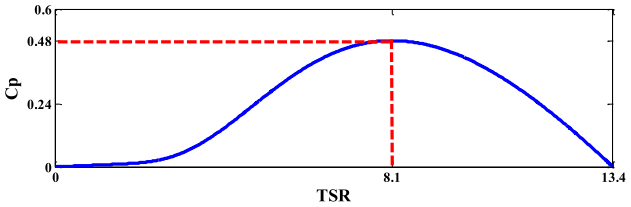

Fig. 4 Power coefficient (C_p) versus the tip speed ratio (λ)

$$\psi_{q3} = L_{q3} i_{q3} \tag{13}$$

$$\psi_{d3} = L_{d3} i_{d3} + \psi_3 \tag{14}$$

where ψ_1 and ψ_3 are the amplitude of odd harmonics components of the permanent magnet flux linkages, respectively.

The electromagnetic torque of five-phase PMSG is given by:

$$T_e = \frac{5}{2} p \left(\psi_{d1} i_{q1} - \psi_{q1} i_{d1} + 3\psi_{d3} i_{q3} - 3\psi_{q3} i_{d3} \right) \tag{15}$$

By eradicating the effect of third harmonic current components and joules losses, the electromagnetic torque becomes:

$$T_e = \frac{5}{2} p \psi_1 i_{q1} \tag{16}$$

The mechanical equation of the WT system is expressed as:

$$T_m = T_e + f\omega_m + J\dot{\omega}_m \tag{17}$$

that f is the friction coefficient and J is the moment of inertia.

3 Machine-side converter

The MSC is applied to obtain the available optimal power from different wind conditions. At MPPT region, the rotor speed should be regulated in order to attain $\lambda_{\text{opt}} = 8.1$and $C_{p\_\text{opt}} = 0.48$ at different wind speed. Figure 5 shows the complete control scheme of the WECS-based large-scale five-phase PMSG that includes the WT connected to the five-phase PMSG, the MSC, the GSC and overall system control. Field-oriented control (FOC) is employed to the MSC by using two control loops, speed control and current control loops. The speed control uses widely PI controller to reduce the error between reference and actual speeds. The reference speed depends on the MPPT that gives the exact value for WT working condition. On the other hand, the current control forces current components (i_{d1}, i_{d3} and i_{q3}) to zero and regulates the q-axis current

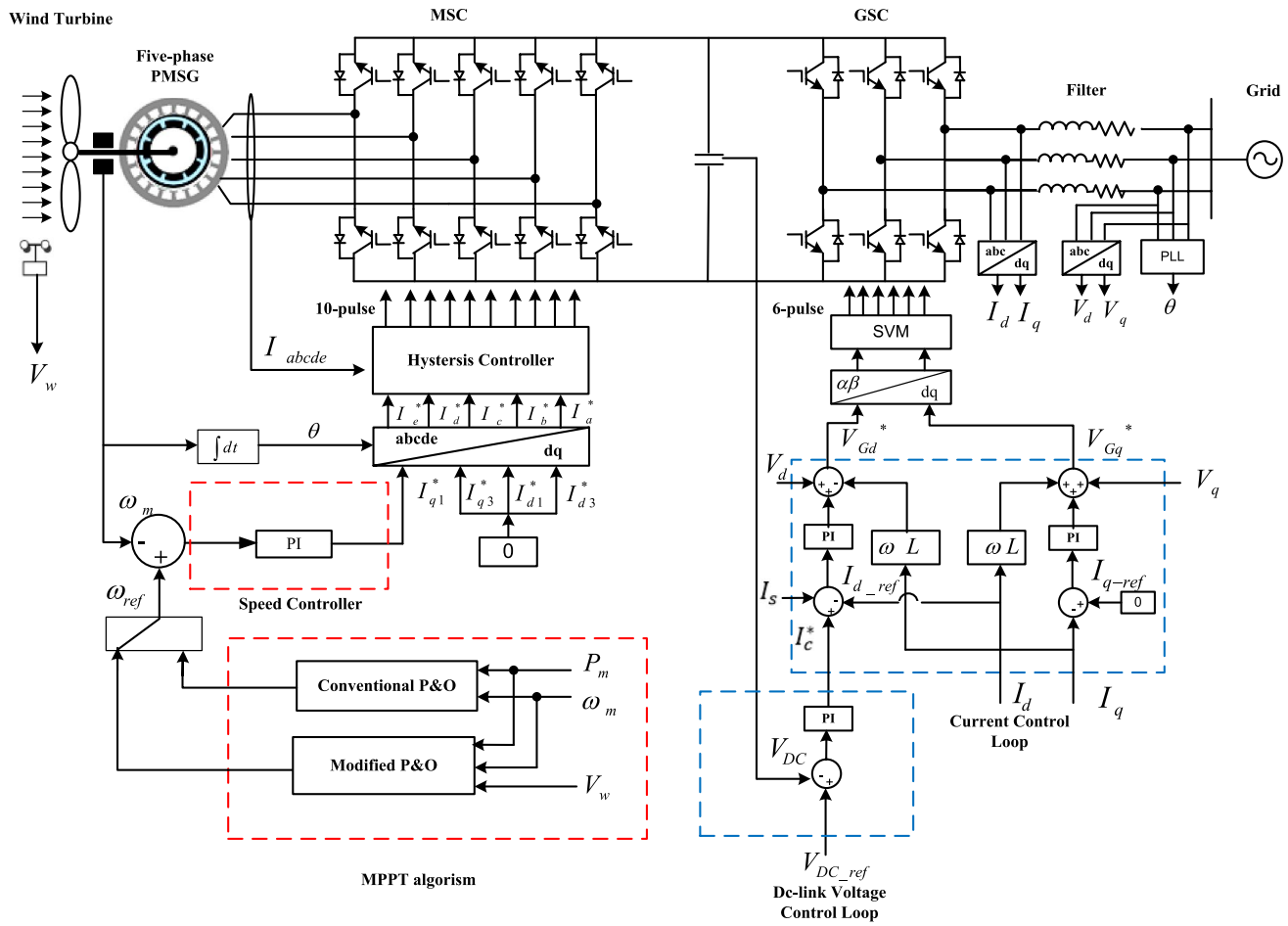

Fig. 5 Control scheme

component (i_{q1}) according to the speed control loop. Hysteresis controller is used to vary switching ratios and produce gate pulses as a response of wind condition variation [5, 16, 42].

4 MPPT control

4.1 Conventional P&O MPPT algorithm

In order to chase the location of the MPP, the CPO MPPT algorithm applies a mathematical optimization technique to achieve the slope of the *P*–*ω* characteristic curve that equals zero. It is simple control method that the prior WT information and an anemometer are not required. In addition, it depends on perturbing the control variables in steps and observing the change in objective function until the MPP is reached at zero slope. In this algorithm, if the operating point is on the left side of the MPP, the CPO controller changes the rotor speed with an increment value to the right. Otherwise, if it locates on the right side, the controller reverses the direction as illustrated in Fig. 6. The WT performance is directly influenced by choosing the perturb step of the CPO. The large step size causes fast tracking of the MPP with small settling time, but it has large oscillations around the MPP, whereas applying the small step size reduces oscillations and improves the MPP reliability; however, it minimizes the speed convergence. The high wind speed fluctuations cause perturbing in the wrong search direction of the MPP. Thus, the CPO control has two serious problems that are related with the rotor speed adjustment efficiency and the wrong direction

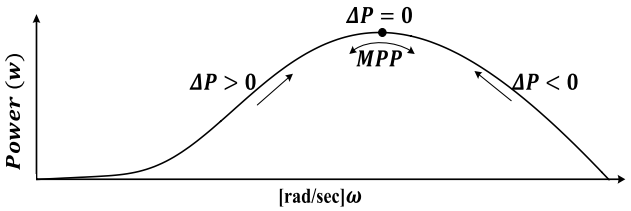

Fig. 6 CPO MPPT controller operation

tracking. These problems reduce the WECS performance, especially at rapid variation, and increase the power losses. To overcome these drawbacks, using the MPO with variable step size, according to variation in environmental conations, is the best control strategy solution. The CPO MPPT controller performance under fixed step size, small step or large step, is depicted in Fig. 7a and b, respectively. Also, Fig. 8 shows the flow chart of the fixed step size algorithm [5, 8, 18, 19].

4.2 Proposed four-sector P&O MPPT technique

The operation of the proposed four-sector algorithm (MPO) depends on the operating power point location on the P_m–ω_m characteristic curve. In order to obtain four sectors, sector 1, sector 2A, sector 2B and sector 3, from the P_m–ω_m characteristic curve, a new proposed curve ($V_{wind} \cdot \Delta P_m/\Delta\omega_m$) is contrasted with the main P_m–ω_m characteristic curve as illustrated in Fig. 9a. Variable-speed step sizes are constructed according to the sector range of the operating point. If the operating point is located in as shown in Fig. 9b:

- Sectors (1 and 3) which are existing far away from the MPP location, the large speed step size is applied.
- Sectors (2A and 2B) which are lying near the MPP location, the small step size is utilized.

The proposed algorithm eliminates drawbacks of the CPO and enhances the WECS performance. The MPO controller maximizes the captured power, improves the settling time and reduces the oscillation level. Figure 10 depicts the proposed algorithm flowchart.

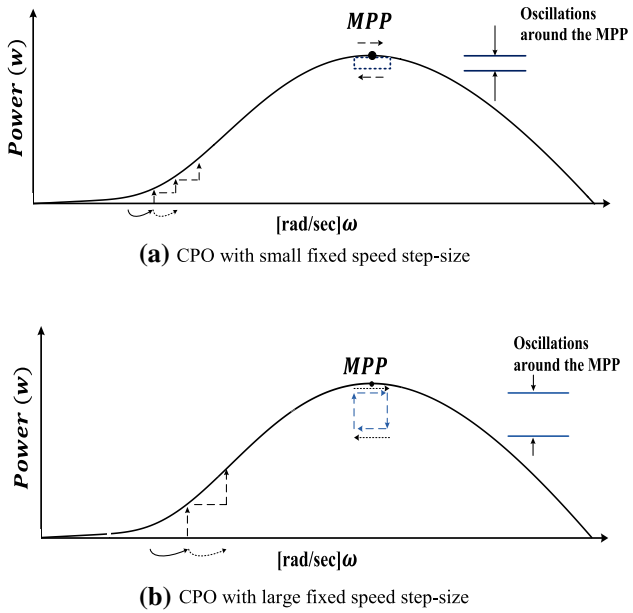

Fig. 7 CPO MPPT algorithm

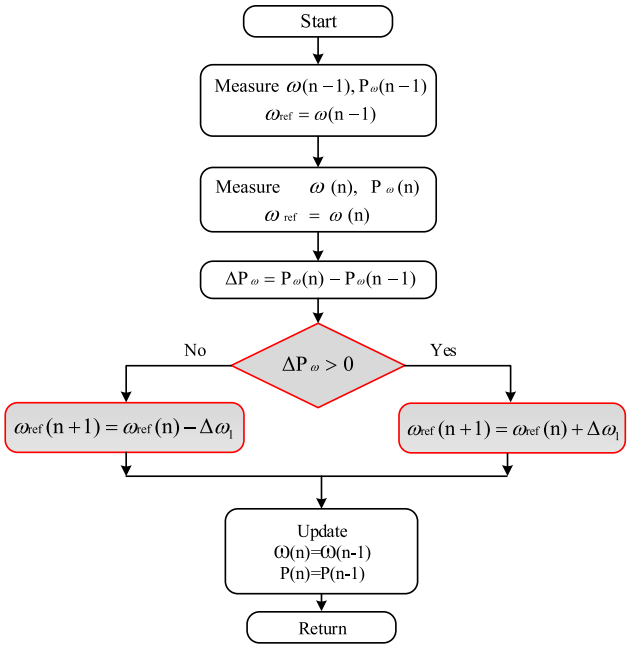

Fig. 8 Flow chart of the CPO MPPT algorithm

4.3 GSC control system

The GSC injects the generated power from the MSC into the utility grid at unity PF, besides regulating the constant voltage of the Dc-link by utilizing a voltage-oriented control (VOC). The VOC includes dual control loops, the outer control loop for adjusting the Dc-link capacitor voltage at constant value and the inner one

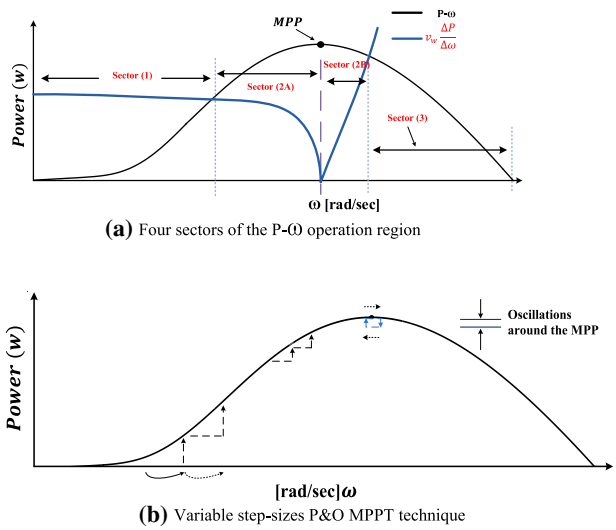

Fig. 9 Modified four-sector P&O MPPT technique

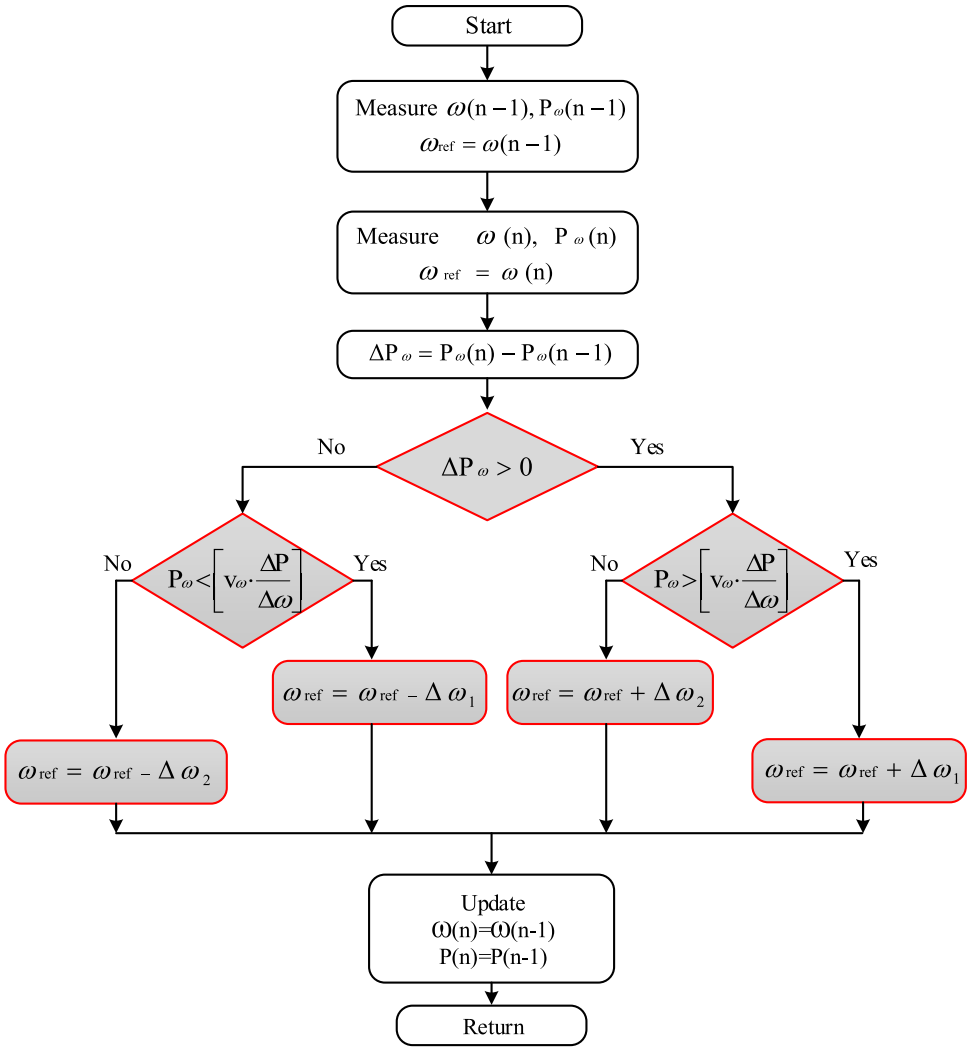

Fig. 10 Flow chart of the modified four-sector P&O MPPT technique

is the responsible of supplying the utility grid with smoothing active power. Voltages at the grid terminals come across the following equations [5, 16, 42, 43]:

$$\begin{bmatrix} V_{ia} \\ V_{ib} \\ V_{ic} \end{bmatrix} = [R_f] \begin{bmatrix} i_{fa} \\ i_{fb} \\ i_{fc} \end{bmatrix} + \begin{bmatrix} \dot{\lambda}_a \\ \dot{\lambda}_b \\ \dot{\lambda}_c \end{bmatrix} + \begin{bmatrix} V_{ga} \\ V_{gb} \\ V_{gc} \end{bmatrix} \tag{18}$$

where R_f and L_f are diagonal matrices, $\dot{\lambda}_a = L_f \frac{\mathrm{d}i_{fa}}{\mathrm{d}t}, \dot{\lambda}_b = L_f \frac{\mathrm{d}i_{fb}}{\mathrm{d}t}$ and $\dot{\lambda}_c = L_f \frac{\mathrm{d}i_{fc}}{\mathrm{d}t}$. The d–q axis voltage components of the GSC are as follows:

$$\begin{bmatrix} V_{id} \\ V_{iq} \end{bmatrix} = [r_f] \begin{bmatrix} i_{fd} \\ i_{fq} \end{bmatrix} + \begin{bmatrix} \dot{\lambda}_{fd} - \omega_g \psi_{fq} \\ \dot{\lambda}_{fq} + \omega_g \psi_{fd} \end{bmatrix} + \begin{bmatrix} V_{gd} \\ V_{gq} \end{bmatrix} \tag{19}$$

where $\omega_g = 2\pi f_g$, $\psi_{fq} = l_f i_{fq}$, $\psi_{fd} = l_f i_{fd}$, $\dot{\lambda}_{fd} = l_f \frac{\mathrm{d}}{\mathrm{d}t} i_{fd}$, $\dot{\lambda}_{fq} = l_f \frac{\mathrm{d}}{\mathrm{d}t} i_{fq}$ and $V_{gq} = 0$ to ensure only active power injection.

The MSC transfers all generated power to the GSC, the Dc-link voltage is controlled to a constant value as:

$$I_c = \frac{P_e - P_g}{V_{dc}} = C \frac{\mathrm{d}V_{dc}}{\mathrm{d}t} \tag{20}$$

that I_c is the capacitor current of the Dc-link, P_e and P_g are output the MSC power and the GSC power, respectively.

$$i_{fd}^* = I_s - I_c^* \quad \text{and} \quad I_s = \frac{P_e}{V_{dc}} \tag{21}$$

where i_{fd}^* and I_c^* are the d-axis current component and the reference current of the capacitor, respectively. Finally, the active power and the reactive power expressions, respectively, are:

$$P_g = \frac{3 V_{gd} i_{fd}}{2} \tag{22}$$

$$Q_g = \frac{3V_{gd}i_{fq}}{2} \quad (23)$$

5 Simulation results and discussion

The effectiveness of proposed MPO algorithm is investigated using step change profile of wind speed change with average speed (10 m/s) as shown in Fig. 11a. The results of the proposed four-sector technique are compared with the conventional P&O, using the small and large fixed step size under climate conditions to reveal the effectiveness of the proposed algorithm. To validate the performance of the proposed MPO algorithm, the theoretical average output power (P_{th}) overall time is compared with the actual grid power integration (P_g) expressed as [41]:

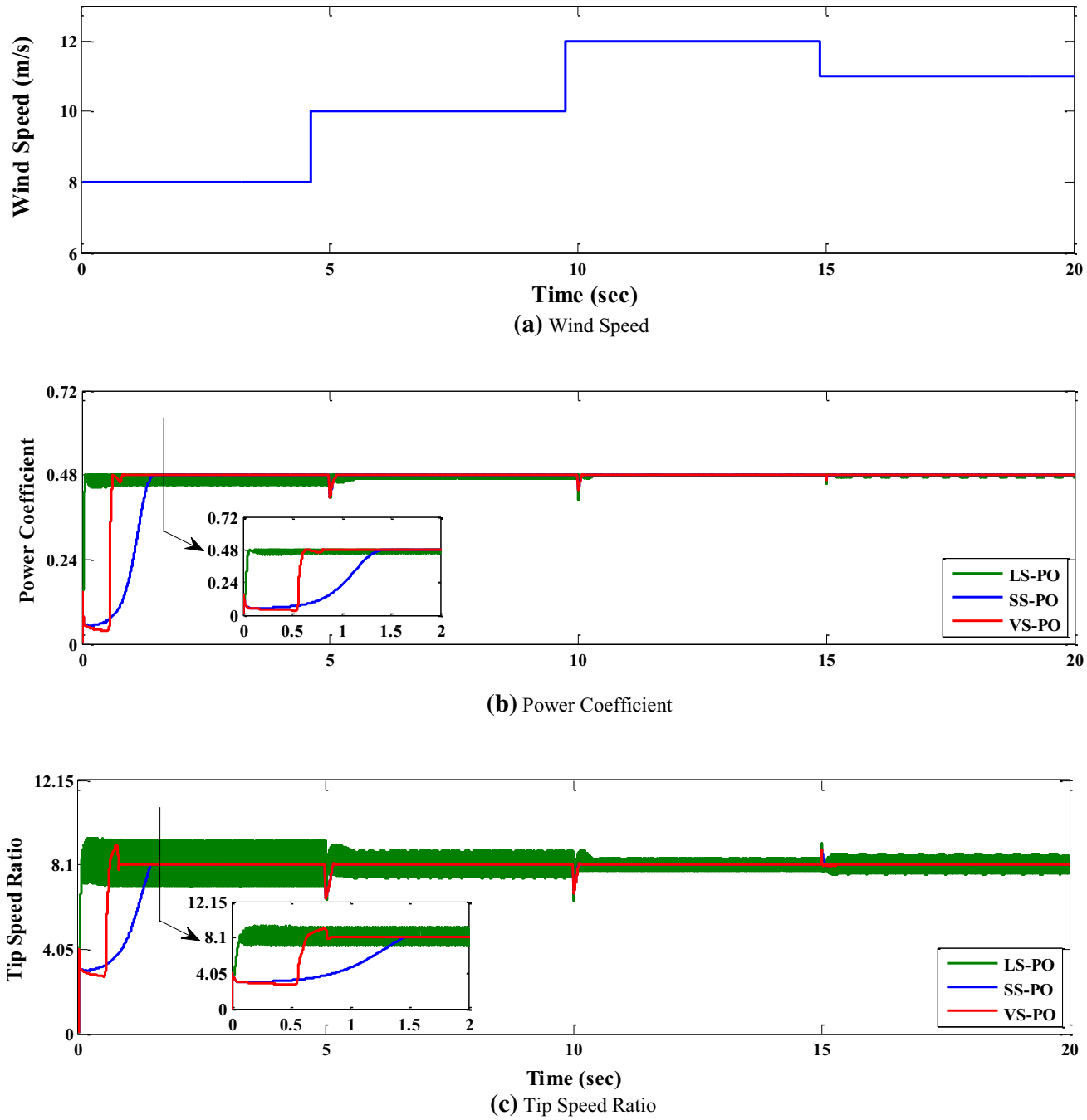

Fig. 11 WT characteristics

$$\eta_{\text{system}} = \frac{\int_0^t P_g \mathrm{d}t}{\int_0^t P_{\text{th}} \mathrm{d}t} \times 100\% \quad (24)$$

The overall WECS parameters are given in "Appendix 1". The influence of the inertia in the dynamic system model is considered in "Appendix 2". The MSC gains and the DC-link and GSC gains are detailed in [17, 20] to obtain the best performance as given in "Appendix 3".

5.1 MSC performance

The proposed MPO algorithm is validated using step wind speed change. The optimal values of the power coefficient and the TSR, 0.48 and 8.1, respectively, are illustrated in Fig. 11b, c. In Fig. 11b, the system response with large step size PO (LS-PO) is the fastest compared to the small step PO (SS-PO), and the MPO, with a settling time of (77 ms). However, LS-PO has high oscillation levels which badly affect the extracted mechanical power and the machine vibration. The SS-PO reduces

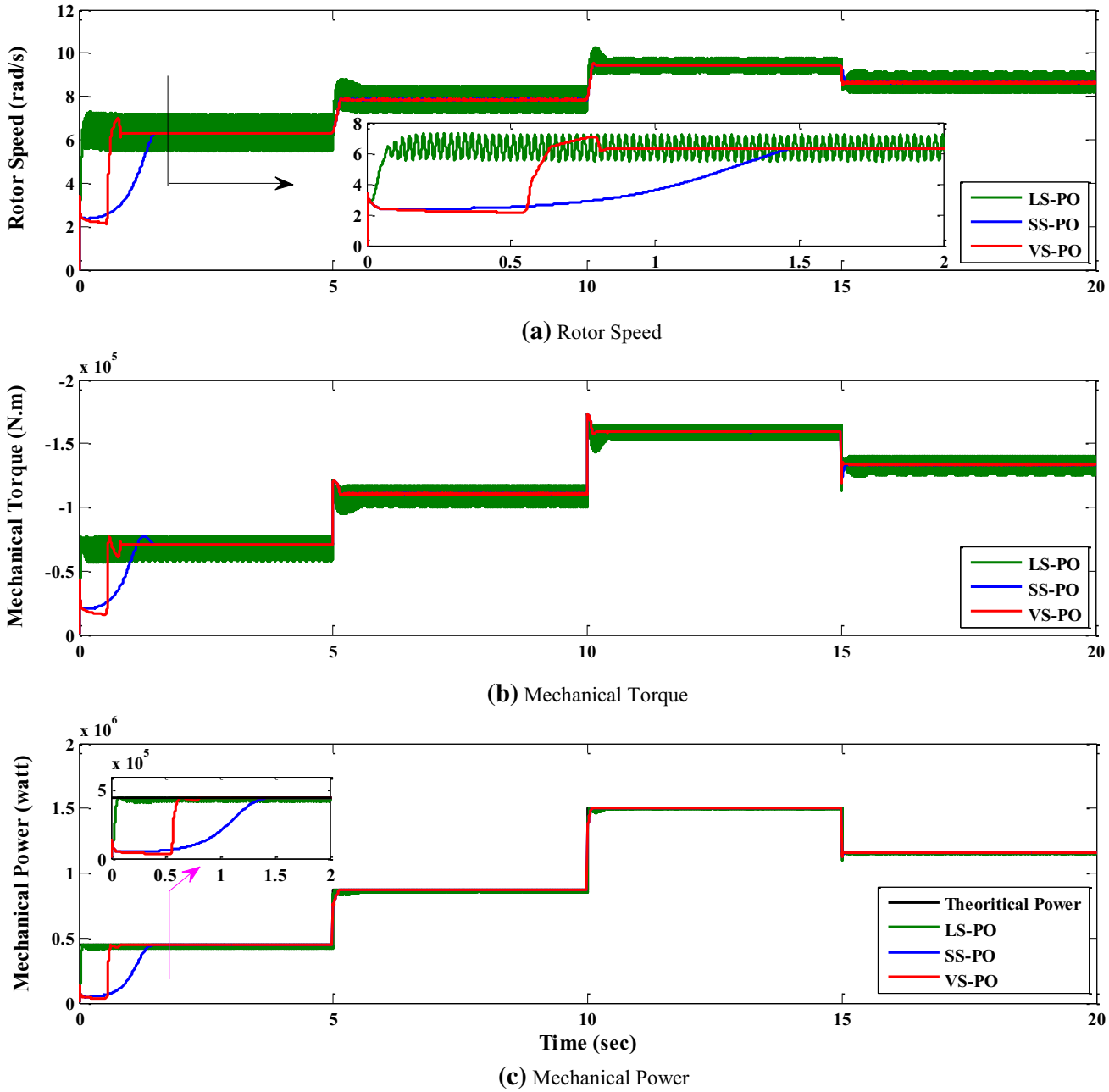

Fig. 12 MSC characteristics

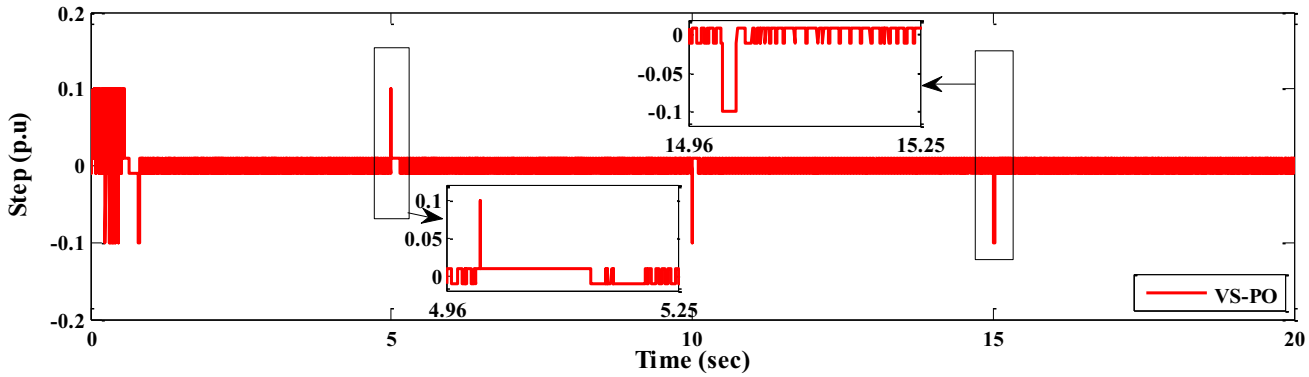

Fig. 13 MPO step size

the large oscillations with small steady-state oscillations. However, the system response is too slow with large settling time (1300 ms). In contrast, the proposed MPO has smallest steady-state oscillations as well as SS-PO and lower settling time of 600 ms. Moreover, the average value of C_p of the proposed MPO algorithm is highest compared with LS-PO and SS-PO. The tip speed ratio is detected at the optimal value (8.1) for conventional, and proposed MPO in Fig. 11c. Moreover, Fig. 12a illustrates that the rotor speed is well-regulated at different wind speeds. The LS-PO has large oscillations (peak-to-peak speed ripples = 1.2 rad/s) and the SS-PO has small steady-state oscillations (peak-to-peak speed ripples = 0.05 rad/s). Moreover, the MPO steady-state oscillations are 0.05 rad/s peak-to-peak speed ripples. The mechanical torque for different algorithms is shown in Fig. 12b. The proposed MPO shows an efficient tracking algorithm compared to the conventional MPPT algorithms. In addition, the proposed MPO extracts the maximum mechanical power more efficient compared to other conventional algorithms as shown in Fig. 12c. To assure the MPO operation, the different step sizes are depicted in Fig. 13.

5.2 GSC performance

On the other hand, the simulation results of the utility grid are shown in Fig. 14. The Dc-link voltage is regulated at constant value (1150 V) as depicted in Fig. 14a. The active power depends upon the *d*-axis current and varies with any change in wind speed as presented in Fig. 14b, c, respectively. Otherwise, the *q*-axis current is forced to zero which makes the reactive power zero, and it is observed that the power factor is unity as clarified in Fig. 14d–f, respectively . The simulation results show the superior performance of the MPO compared with the CPO. The MPO enhances the system efficiency from 87% in the SS-PO to 90%. It is clear that the MPO enhances the overall efficiency and eradicates the limitations of the conventional PO techniques as summarized in Table 1.

6 Conclusion

The proposed MPO MPPT algorithm is investigated as an efficient MPPT method that eliminates the speed oscillations and improves the tracking speed. It is simple and less complexity than other CPO methods. The strategy depends on the idea of dividing the power-speed curve into four sectors by comparing the power-speed curve and a newly synthesized curve. The variety of the operating step size is related to the position of the operating point in which sector. For the sectors close to the MPP, small step size is applied. Otherwise, a large step size is applied. The proposed MPO algorithm exhibits high efficiency and fast response at different environmental conditions. By utilizing the proposed MPO algorithm, the loss of tracking and wrong directionally problems are avoided. Moreover, the dynamic tracking performance is enhanced by accurately attainting the MPP with high performance, either in the transient or in the steady-state conditions. To confirm the superiority of the proposed algorithm, the proposed MPO algorithm is compared with the conventional P&O MPPT algorithm. The proposed MPO MPPT hunts the MPP more efficient with low steady-state oscillations which increases the overall WECS efficiency from 87 to 90%. The study is based on a large-scale five-phase PMSG with grid tied for WECS. The MSC is implemented to

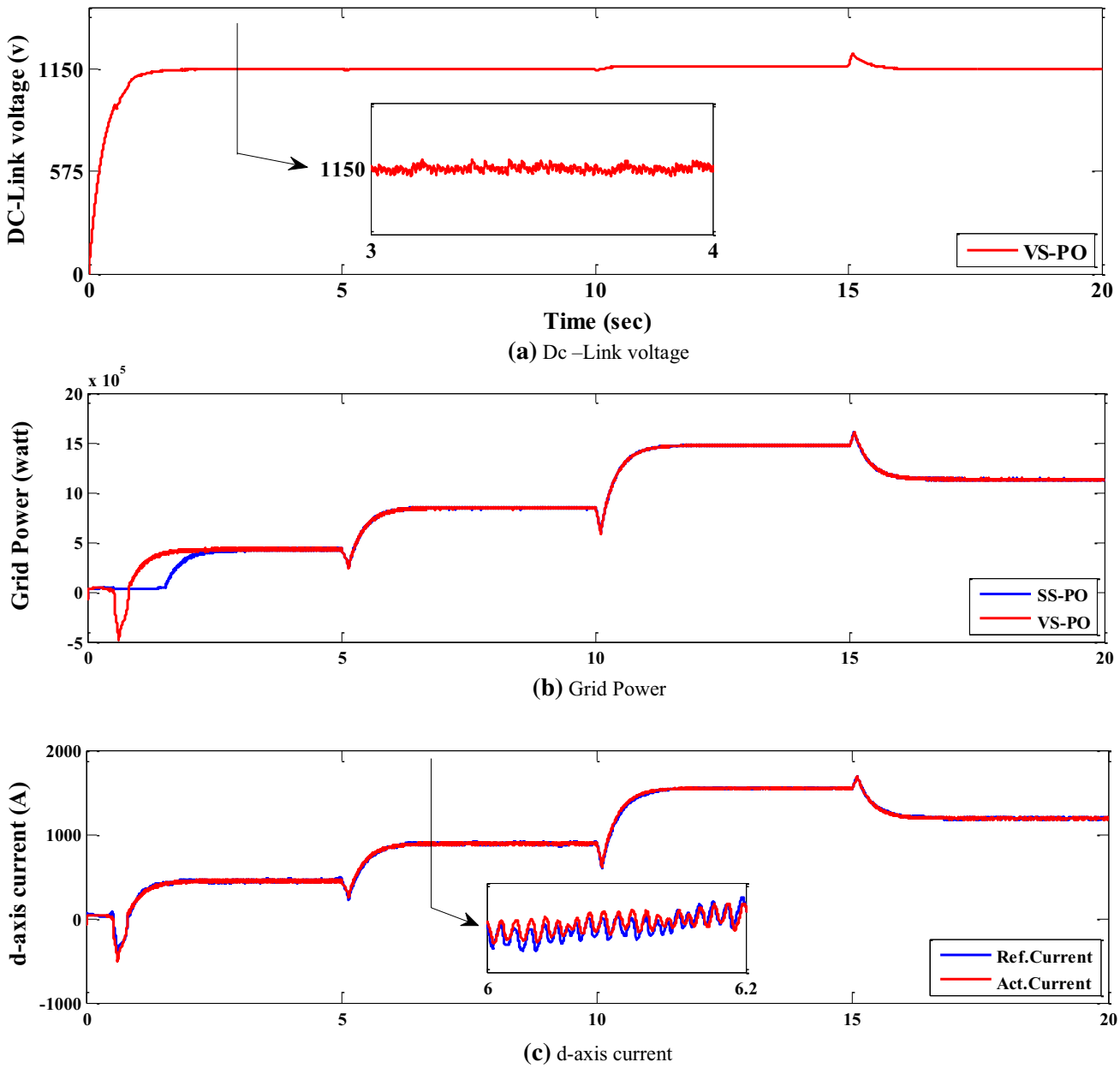

Fig. 14 GSC characteristics

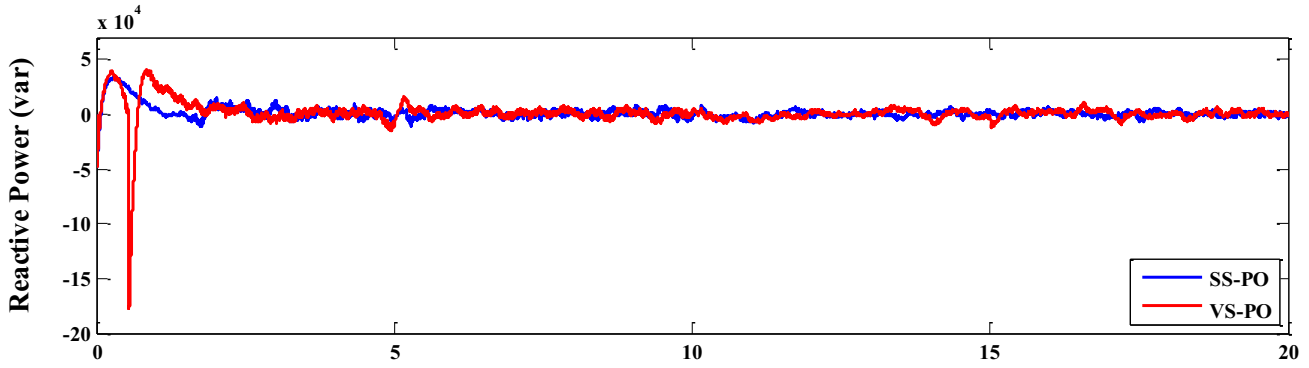

(d) Reactive Power

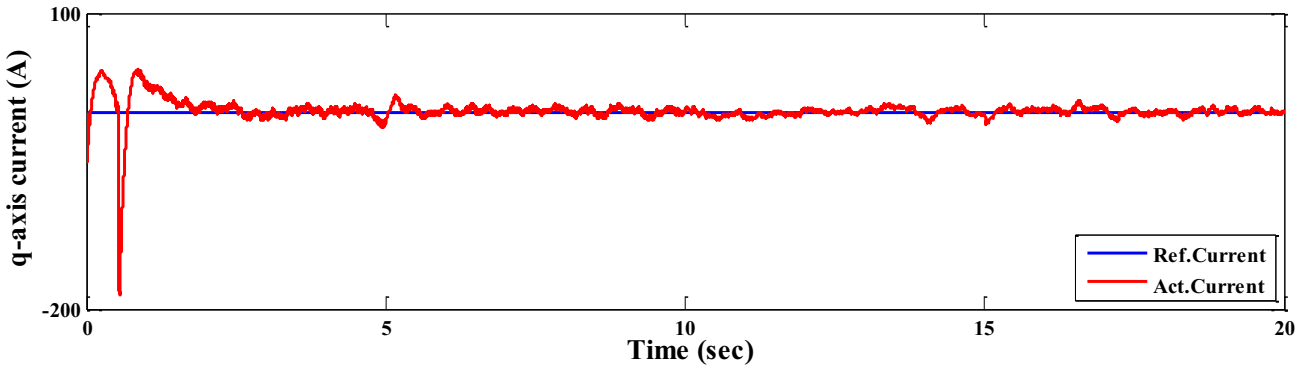

(e) d-axis current

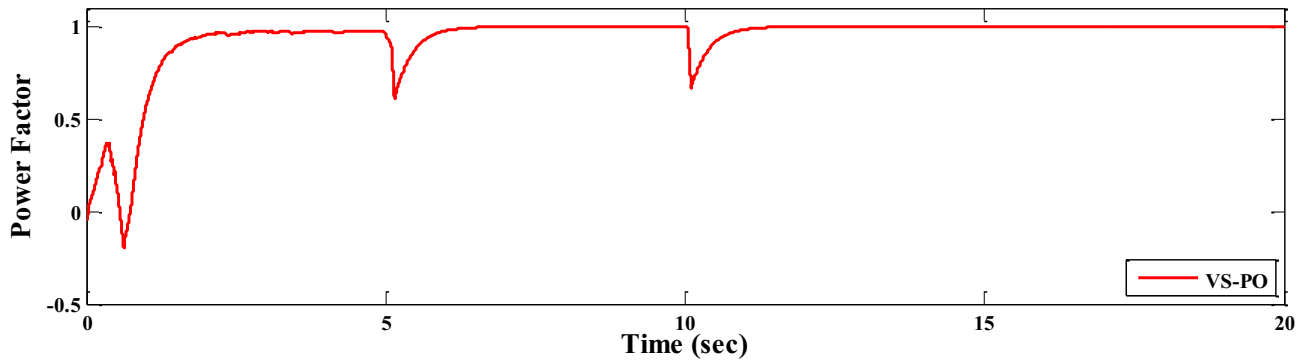

(f) Power Factor

Fig. 14 (continued)

Table 1 Comparison between the conventional and proposed P&O MPPT technique for WECS

MPPT algorithm	Speed ripple (P. P) (rad/s)	$\Delta\omega$ (rad/s)	Settling time (ms)	η_{sys}
Conventional large fixed step P&O	1.2	$\Delta\omega_1 = 0.1$	77	–
Conventional small fixed step P&O	0.05	$\Delta\omega_1 = 0.01$	1300	87%
Proposed four-sector P&O	0.05	$\Delta\omega_1 = 0.1$ $\Delta\omega_2 = 0.01$	600	90%

extract the optimal power also the GSC is used as Dc-link voltage regulator and for unity power factor injection at any wind speed. Simulation results of the proposed algorithm are confirmed using MATLAB/SIMULINK program.

Acknowledgements The authors thank their colleagues who provided insight and expertise that greatly assisted the research.

Compliance with ethical standards

Conflict of interest The authors declare that they have no conflict of interest.

Appendix 1

WECS parameters [40, 44].

Specification of wind turbine

The coefficients C_1–C_6	$C_1 = 0.5176$	$C_2 = 116$	$C_3 = 0.4$
	$C_4 = 5$	$C_5 = 21$	$C_6 = 0.0068$
Blade radius	$R = 35.25$ m		
Air density	$\rho = 1.225$ kg/m^3		
Optimal tip speed ratio	$\lambda_{opti} = 8.1$		
Maximum power coefficient	$C_{p-max} = 0.48$		

Five-phase PMSG parameters

Rated power	$P = 1.5$ MW
Pole pairs number	$n_p = 40$
Stator resistance	$R_s = 3.17$ mΩ
Stator inductance	$L_s = 3.07$ mH
Moment of inertia	$J = 10,000$ kg m^2
Flux linkage	$\psi = 7.0172$ wb

DC bus and gird parameters

Dc-link voltage	$V_{dc} = 1150$ V
Capacitor of the dc-link	$C = 0.023$ F
Grid voltage	$V_g = 575$ V
Grid frequency	$F = 60$ Hz
Grid resistance	$R_g = 0.003$ pu
Grid inductance	$L_g = 0.3$ pu

Appendix 2

Influence of inertia on electromagnetic torque [45]:

$$T_e \pm T_m = f\omega_m + J\dot{\omega}_m \tag{25}$$

(−) sign and (+) sign for acceleration mode and deceleration mode, respectively.

Acceleration mode $\left(\Delta\omega/\Delta t > 0\right)$

$$T_e - T_m = f\omega_m + J\dot{\omega}_m \tag{26}$$

In step change $\Delta t \rightarrow 0$ very small value, so

$$T_e \uparrow\uparrow \propto J \uparrow \frac{d\omega_m}{dt \downarrow\downarrow} \propto J\frac{\Delta\omega_m}{\Delta T} \tag{27}$$

Deceleration mode $\left(\Delta\omega/\Delta t < 0\right)$

$$T_e + T_m = f\omega_m + J\dot{\omega}_m \tag{28}$$

and

$$T_e \downarrow\downarrow \propto J \uparrow \frac{d\omega_m}{dt \downarrow\downarrow} \propto J\frac{\Delta\omega_m}{\Delta T} \tag{29}$$

where $\Delta\omega = \omega_{new} - \omega_{old}$.

Appendix 3

PI controller gains.

Speed controller at the MSC [46]

K_p	5
K_i	15

The GSC gains [47]

Dc-link control	$K_{p\_V_{dc}}$	8
	$K_{i\_V_{dc}}$	400
D-axis current control	K_{p_id}	0.83
	K_{i_id}	5
Q-axis current control	K_{p_iq}	0.83
	K_{i_iq}	5

References

1. Kaldellis J, Apostolou D (2017) Life cycle energy and carbon footprint of offshore wind energy. Comparison with onshore counterpart. Renew Energy 108:72–84

2. Aliyu AK, Modu B, Tan CW (2018) A review of renewable energy development in Africa: a focus in South Africa, Egypt and Nigeria. Renew Sustain Energy Rev 81:2502–2518
3. Hossain MM, Ali MH (2015) Future research directions for the wind turbine generator system. Renew Sustain Energy Rev 49:481–489
4. Xie D, Lu Y, Sun J, Gu C (2017) Small signal stability analysis for different types of PMSGs connected to the grid. Renew Energy 106:149–164
5. Tripathi S, Tiwari A, Singh D (2015) Grid-integrated permanent magnet synchronous generator based wind energy conversion systems: a technology review. Renew Sustain Energy Rev 51:1288–1305
6. Li H, Chen Z (2008) Overview of different wind generator systems and their comparisons. IET Renew Power Gener 2:123–138
7. Islam MR, Guo Y, Zhu J (2014) A review of offshore wind turbine nacelle: technical challenges, and research and developmental trends. Renew Sustain Energy Rev 33:161–176
8. Linus RM, Damodharan P (2015) Maximum power point tracking method using a modified perturb and observe algorithm for grid connected wind energy conversion systems. IET Renew Power Gener 9:682–689
9. Singh G (2002) Multi-phase induction machine drive research—a survey. Electr Power Syst Res 61:139–147
10. Levi E, Bojoi R, Profumo F, Toliyat H, Williamson S (2007) Multiphase induction motor drives–a technology status review. IET Electr Power Appl 1:489–516
11. Reusser CA, Kouro S, Cardenas R (2015) Dual three-phase PMSG based wind energy conversion system using 9-switch dual converter. In: Energy conversion congress and exposition (ECCE), 2015. IEEE, pp 1021–1022
12. Dabour SM, Abdel-Khalik AS, Ahmed S, Massoud A.M. (2017) A new dual series-connected Nine-Switch Converter topology for a twelve-phase induction machine wind energy system. In: 2017 11th IEEE international conference on compatibility, power electronics and power engineering (CPE-POWERENG), pp 139–144
13. Nahome AA, Zaimeddine R, Liu B, Undeland T (2011) Vector control of direct drive six phase permanent magnet synchronous generators. In: 2011 IEEE Trondheim, PowerTech, pp 1–7
14. Abdelsalam I, Adam G, Holliday D, Williams B (2013) Assessment of a wind energy conversion system based on a six-phase permanent magnet synchronous generator with a twelve-pulse PWM current source converter. In: 2013 IEEE, ECCE Asia Downunder (ECCE Asia), pp 849–854
15. Liang C, Le Claire J-C, Aït-Ahmed M, Benkhoris M-F (2017) Power control of 5-phase PMSG-diode rectifier-interleaved Boost set under health and fault modes. Electr Power Syst Res 152:316–322
16. Youssef A-R, Sayed MA, Abdelwhab MN, Shabib G (2016) Generator side converter for five-phase PMSG based wind turbine generators using perturbation and observation technique. Int J Power Eng Energy (IJPEE) 7:610–618
17. Mousa HHH, Youssef A-R, Mohamed EEM (2019) Model predictive speed control of five-phase permanent magnet synchronous generator-based wind generation system via wind-speed estimation. Int Trans Electr Energy Syst 29(5):e2826
18. Kumar D, Chatterjee K (2016) A review of conventional and advanced MPPT algorithms for wind energy systems. Renew Sustain Energy Rev 55:957–970
19. Abdullah MA, Yatim A, Tan CW, Saidur R (2012) A review of maximum power point tracking algorithms for wind energy systems. Renew Sustain Energy Rev 16:3220–3227
20. Mousa HH, Youssef A-R, Mohamed EE (2018) Model Predictive Speed Control of Five-Phase PMSG Based Variable Speed Wind Generation System. In 2018 Twentieth international middle east power systems conference (MEPCON), pp 304–309
21. Morimoto S, Nakayama H, Sanada M, Takeda Y (2005) Sensorless output maximization control for variable-speed wind generation system using IPMSG. IEEE Trans Ind Appl 41:60–67
22. Zhao Y, Wei C, Zhang Z, Qiao W (2013) A review on position/speed sensorless control for permanent-magnet synchronous machine-based wind energy conversion systems. IEEE J Emerg Sel Top Power Electr 1:203–216
23. Safari A, Mekhilef S (2011) Simulation and hardware implementation of incremental conductance MPPT with direct control method using cuk converter. IEEE Trans Ind Electron 58:1154–1161
24. Mei Q, Shan M, Liu L, Guerrero JM (2011) A novel improved variable step-size incremental-resistance MPPT method for PV systems. IEEE Trans Ind Electron 58:2427–2434
25. Carrillo C, Montaño AO, Cidrás J, Díaz-Dorado E (2013) Review of power curve modelling for wind turbines. Renew Sustain Energy Rev 21:572–581
26. Abdullah M, Yatim A, Tan C (2014) An online optimum-relation-based maximum power point tracking algorithm for wind energy conversion system. In: 2014 Australasian universities power engineering conference (AUPEC), pp 1–6
27. Femia N, Granozio D, Petrone G, Spagnuolo G, Vitelli M (2007) Predictive & adaptive MPPT perturb and observe method. IEEE Trans Aerosp Electron Syst 43(3):934–950
28. Kazmi SMR, Goto H, Guo H-J, Ichinokura O (2011) A novel algorithm for fast and efficient speed-sensorless maximum power point tracking in wind energy conversion systems. IEEE Trans Ind Electron 58:29–36
29. Harrag A, Messalti S (2015) Variable step size modified P&O MPPT algorithm using GA-based hybrid offline/online PID controller. Renew Sustain Energy Rev 49:1247–1260
30. Wang Q, Chang L (2004) An intelligent maximum power extraction algorithm for inverter-based variable speed wind turbine systems. IEEE Trans Power Electron 19:1242–1249
31. González L, Figueres E, Garcerá G, Carranza O (2010) Maximum-power-point tracking with reduced mechanical stress applied to wind-energy-conversion-systems. Appl Energy 87:2304–2312
32. Agarwal V, Aggarwal RK, Patidar P, Patki C (2010) A novel scheme for rapid tracking of maximum power point in wind energy generation systems. IEEE Trans Energy Convers 25:228–236
33. Dalala ZM, Zahid ZU, Yu W, Cho Y, Lai J-SJ (2013) Design and analysis of an MPPT technique for small-scale wind energy conversion systems. IEEE Trans Energy Convers 28:756–767
34. Kortabarria I, Andreu J, de Alegría IM, Jiménez J, Gárate JI, Robles E (2014) A novel adaptative maximum power point tracking algorithm for small wind turbines. Renew Energy 63:785–796
35. Putri RI, Pujiantara M, Priyadi A, Ise T, Purnomo MH (2017) Maximum power extraction improvement using sensorless controller based on adaptive perturb and observe algorithm for PMSG wind turbine application. IET Electr Power Appl 12:455–462
36. Mousa HH, Youssef A-R, Mohamed EE (2019) Variable step size P&O MPPT algorithm for optimal power extraction of multi-phase PMSG based wind generation system. Int J Electr Power Energy Syst 108:218–231
37. Mousa HHH, Youssef A-R, Mohamed EEM (2019) Study of robust adaptive step-sizes P&O MPPT algorithm for high-inertia WT with direct-driven multiphase PMSG. Int Trans Electr Energ Syst. https://doi.org/10.1002/2050-7038.12090
38. Uddin MN, Amin IK (2019) Adaptive step size based hill-climb search algorithm for MPPT control of DFIG-WECS with reduced power fluctuation and improved tracking performance. Electr Power Compon Syst 49:2203–2214

39. Karabacak M (2019) A new perturb and observe based higher order sliding mode MPPT control of wind turbines eliminating the rotor inertial effect. Renew Energy 133:807–827
40. Yang B, Yu T, Shu H, Zhang Y, Chen J, Sang Y, Jiang L (2018) Passivity-based sliding-mode control design for optimal power extraction of a PMSG based variable speed wind turbine. Renew Energy 119:577–589
41. Mousa HHH, Youssef A-R, Mohamed EEM (2019) Optimal power extraction control schemes for five-phase PMSG based wind generation systems. Eng Sci Technol Int J. https://doi.org/10.1016/j.jestch.2019.04.004
42. Athari H, Niroomand M, Ataei M (2017) Review and classification of control systems in grid-tied inverters. Renew Sustain Energy Rev 72:1167–1176
43. Barros L, Barros C (2017) An internal model control for enhanced grid-connection of direct-driven PMSG-based wind generators. Electr Power Syst Res 151:440–450
44. Nasiri M, Milimonfared J, Fathi S (2015) A review of low-voltage ride-through enhancement methods for permanent magnet synchronous generator based wind turbines. Renew Sustain Energy Rev 47:399–415
45. Dabrowski M (2010) Permanent magnet motor technology: design and applications. ed: Wydawnictwo SIGMA-NOT Sp Zoo ul Ratuszowa 11, PO Box 1004, 00-950 Warsaw, Poland
46. Rahimi M (2017) Modeling, control and stability analysis of grid connected PMSG based wind turbine assisted with diode rectifier and boost converter. Int J Electr Power Energy Syst 93:84–96
47. Shehata E (2017) A comparative study of current control schemes for a direct-driven PMSG wind energy generation system. Electr Power Syst Res 143:197–205